# First hafnium-based MAX phase in the 312 family, Hf3AlC2: A first-principles study


## Author

Roknuzzaman, M, Hadi, MA, Ali, MA, Hossain, MM, Jahan, N, Uddin, MM, Alarco, JA, Ostrikov, K



## Published

2017

## Journal Title

Journal of Alloys and Compounds

## Version

Accepted Manuscript (AM)

## DOI

10.1016/j.jallcom.2017.08.151

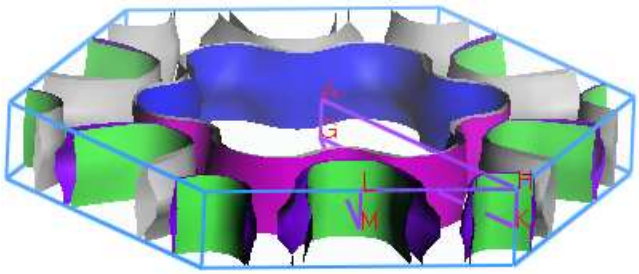
Γ
L
H
M
K

# First hafnium-based MAX phase in the 312 family, $Hf_3AlC_2$: A first-principles study

M. Roknuzzaman[a], M.A. Hadi[b1], M.A. Ali[c], M.M. Hossain[c], N. Jahan[c], M.M. Uddin[c], J.A. Alarco[a,d1], K. Ostrikov[a]

[a]*School of Chemistry, Physics and Mechanical Engineering, Queensland University of Technology, QLD 4000, Australia*
[b]*Department of Physics, University of Rajshahi, Rajshahi 6205, Bangladesh*
[c]*Department of Physics, Chittagong University of Engineering and Technology, Chittagong 4349, Bangladesh*
[d]*Institute for Future Environments, Queensland University of Technology, QLD 4000, Australia*

## ABSTRACT

The ground state physical properties of the newly synthesized 312 MAX compound, $Hf_3AlC_2$ have been investigated using the first-principles density functional theory (DFT). The optimized unit cell parameters show good agreement with the experimental values. The calculated elastic constants and phonon dispersion confirm the mechanical and dynamical stabilities of this new compound. High bulk modulus, combined with low shear resistance and low Vickers hardness, indicates good machinability of $Hf_3AlC_2$, as expected for a metallic compound. On the other hand, significant stiffness due to large Young's modulus as well as the brittle nature according to the calculated Pugh's and Poison's ratios and Cauchy pressure are comparable to that of a ceramic. The present calculations show that $Hf_3AlC_2$ is elastically and optically anisotropic. The chemical bonding in $Hf_3AlC_2$ consists of a mixture of metallic, covalent and ionic contributions. The calculated Fermi surface contains quasi-two-dimensional topology, which indicates possible superconductivity of $Hf_3AlC_2$. The new phase $Hf_3AlC_2$ may also be a promising thermal barrier coating (TBC) material. The calculated enthalpy and entropy are found to increase with temperature above 100 K though a decrease is observed for the free energy.

**Keywords:** $Hf_3AlC_2$ MAX-phase; DFT calculations; Physical properties.

## 1. Introduction

Over the last two decades, the scientific community has paid huge attention to the nanolaminates known as MAX phases with chemical formula $M_{n+1}AX_n$ ($n$ = 1-3) [1], where M stands for an early transition metal, A refers to an A-group element and X represents carbon and/or nitrogen. The MAX phases take shape of hexagonal structure with space group $P6_3/mmc$ (No. 194), where the ceramic '$M_{n+1}X_n$' layers are intercalated with metallic planes of the A-element [1-5]. The MAX phases are unparalleled compounds due to their unusual properties attributed from the combination of metallic and ceramic characteristics [1]. Their metallic like properties, for example machinability, damage tolerance, thermal and electrical conductivities make them industrially relevant materials. At the same time, they possess high elastic stiffness, refractory nature and resistance to high-temperature oxidation, just like engineering ceramics [6].

The recent discovery of a magnetic MAX phase has extended the list of interesting properties of MAX family [7]. To date, a large number of MAX phase compounds have been synthesized [8-17] and their physical properties have also been studied [18-27]. Very recently, Lapauw *et al*. has synthesized $Hf_3AlC_2$ [28], which is the first member of 312 MAX phases in the Hf-Al-C system. This phase was first predicted theoretically in 2010 and its elastic and electronic properties were investigated [29]. However, many physical properties like the Debye temperature, Vickers hardness, phonon dispersion, Mulliken population analysis, charge density and Fermi surface, as well as thermodynamic and optical properties, remain unexplored. Investigations of optical functions serve as powerful tools for analyzing the electronic characteristics of solids. Nowadays, during design of new optoelectronic devices, knowledge of absorption coefficient and refractive indices is essential [30]. Microelectronic devices for next generation applications require highly dielectric materials for reduced gate insulators [31]. Moreover, MAX phases are predicted to be potential coating materials for spacecraft to reduce solar heating significantly [32]. Once more, the thermodynamic properties can broaden our knowledge on particular behavior of solids under high pressures and temperatures, which are essential for industrial applications [33]. So, we have aimed at determining the thermodynamic and optical properties of the newly synthesized MAX phase $Hf_3AlC_2$ including Mulliken population analysis, theoretical Vickers hardness, phonon dispersion, charge density and Fermi surface for the

[1]Corresponding author: email address: hadipab@gmail.com (M.A. Hadi),
jose.alarco@qut.edu.au (J.A. Alarco)

first time. To make the present study a complete one, we revisit some features of the elastic and electronic properties.

The arrangement of the rest of this paper is in this way: A concise description of the computational methods carried out here is presented in Section 2. The obtained results are presented and analyzed in Section 3. A brief summary of the findings with concluding remarks is included in Section 4.

## 2. Computational Methods

First principles density-functional theory (DFT) [34,35] calculations are carried out using the Cambridge Serial Total Energy Package (CASTEP) module embodied in Materials Studio 2017 [36]. The generalized gradient approximation (GGA) of Perdew-Burke-Ernzerhof known as the PBE-GGA scheme [37] is used to evaluate the electronic exchange and correlation energy. The electrostatic interaction between valence electron and ionic core is represented by the Vanderbilt-type ultrasoft pseudopotentials [38]. The cutoff energy of 400 eV is used for the expansion of the plane waves. A *k*-point mesh of 27×27×4 according to the Monkhorst-Pack scheme [39] is used for integration over the first Brillouin zone. The algorithm proposed by Broyden *et al*. [40] is applied to configure the atomic position and the density mixing scheme is used to optimize the electronic structure. Reasonable convergence is assured by testing the Brillouin zone sampling and the kinetic energy cutoff with convergence thresholds of $5.0\times10^{-7}$ eV/atom for the tolerance of self-consistent field, $5.0\times10^{-6}$ eV/atom for the energy, 0.01 eV/Å for the maximum force, $5.0\times10^{-4}$ Å for the maximum displacement and 0.02 GPa for the maximum stress, respectively.

## 3. Results and Discussion

### *3.1. Structural properties*

Similar to other MAX phases, $Hf_3AlC_2$ belongs to the $P6_3/mmc$ space group with hexagonal structure. It contains 12 atoms and two formula units in each unit cell. In the optimized structure (Fig. 1), the Wyckoff positions 2*a* and 4*f* with the relevant fractional coordinates (0, 0, 0) and (2/3, 1/3, 0.1325) are occupied by the Hf atoms. The Al atoms take position at 2*b* Wyckoff site with the fractional coordinates (0, 0, 1/4). The C atoms reside in the 4*f* Wyckoff positions with the fractional coordinates (1/3, 2/3, 0.0709). The calculated, geometry optimized unit cell parameters are listed in Table 1 along with corresponding experimental and available theoretical values. Our calculated values are in good agreement with those obtained experimentally [28] as well as with those predicted theoretically before the synthesis of the compound [29,41].

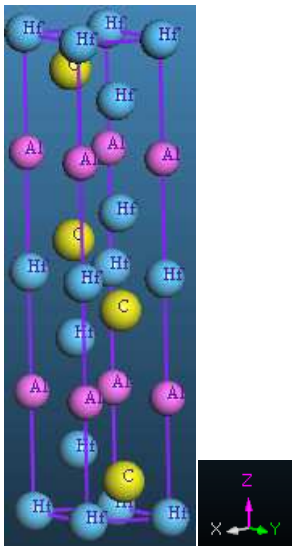


**Fig. 1.** Crystal structure of $Hf_3AlC_2$.

**Table 1.** Optimized lattice parameters *a* and *c* (Å), hexagonal ratio *c/a*, internal parameters $z_{Hf}$ and $z_c$ and unit cell volume *V* (Å$^3$**)** of the $Hf_3AlC_2$ MAX phase.

| *a* | *c* | *c/a* | $z_{Hf}$ | $z_C$ | *V* | Ref. |
|---|---|---|---|---|---|---|
| 3.3320 | 19.6895 | 5.9092 | 0.1325 | 0.0709 | 189.31 | Theo. [This] |
| 3.2844 | 19.6600 | 5.9858 | 0.1307 | – – | 183.66 | Expt. [28] |
| 3.3176 | 19.5160 | 5.8827 | 0.1331 | 0.0712 | 186.03 | Theo. [29] |
| 3.2890 | 19.6820 | 5.8942 | – – | – – | 184.39 | Theo. [41] |

### *3.2. Mechanical properties*

#### *3.2.1. Elastic properties*

Elastic properties are of great interest as they can evaluate numerous essential macroscopic properties of solids. The MAX phases, as hexagonal crystals, own five independent elastic tensors, namely $C_{11}$, $C_{12}$, $C_{13}$, $C_{33}$, and $C_{44}$. These constants are determined with the 'stress-strain' method [42] as compiled in the CASTEP code. The polycrystalline elastic parameters are derived from the single crystal elastic constants applying the Voigt-Reuss-Hill approximations [43–45]. The calculated elastic properties are listed in Table 2 along with those obtained from other calculations [29,41]. Comparison of the present results with the previous data shows a reasonable level of agreement. The independent elastic tensors can be used to judge the mechanical stability of crystal systems. Hexagonal crystals like MAX phases for being mechanically stable, the following criteria based on elastic constants have to be obeyed: $C_{11} > 0$, $C_{11} - C_{12} > 0$, $C_{44} > 0$, $(C_{11} + C_{12})\, C_{33} - 2C_{13}C_{13} > 0$ [46]. Our calculated elastic constants, shown in Table 2, completely satisfy these conditions, indicating the mechanical stability of $Hf_3AlC_2$.

The elastic tensors can also give information about the bonding nature of solids. The bonding strength along the [100] direction is stronger than that of the [001] direction from the fact that $C_{11} > C_{33}$. It means that the new nanolaminate $Hf_3AlC_2$ is harder to compress along the crystallographic *a*-axis, than along the *c*-axis. In addition, $C_{11} > C_{33}$ is the general trend in MAX phase carbides and reveals the anisotropic nature of the compound. Again, $C_{11} + C_{12} > C_{33}$, implies that the bonding strength and tensile elastic modulus in the (001) plane is higher than that along the *c*-axis. The pure shear elastic constant $C_{44}$ assesses the resistance to shear distortion in the (001) plane. It is less than both the unidirectional elastic constants $C_{11}$ and $C_{33}$, indicating that the shear deformation is easier than the linear compression along the crystallographic *a*- and *c*-axes. The elastic constant $C_{66}$ [= $(C_{11} - C_{12})/2$] estimates the resistance to shear distortion in the ⟨110⟩ direction. As $C_{66}$ (135 GPa) > $C_{44}$ (127 GPa), the resistance to shear distortion should be significant in the ⟨110⟩ direction compared to that in the (001) plane for the 312 MAX compound $Hf_3AlC_2$.

The difference, $(C_{12} - C_{44})$, known as the Cauchy pressure, presumes the bonding nature in solids. Metallic bonding dominates in a crystal if its Cauchy pressure is positive, while the material is characterized by directional covalent bonding in case of a negative Cauchy pressure [47]. With a large negative Cauchy pressure of –50 GPa, $Hf_3AlC_2$ should be dominated by directional covalent bonding. The negative Cauchy pressure also indicates a brittle nature for $Hf_3AlC_2$. The elastic constants $C_{12}$ and $C_{13}$ are found to be similar. These two factors combine an applied stress component along the *a*-axis with a uniaxial strain in the *b*- and *c*-axis, respectively. The comparatively small values of $C_{12}$ and $C_{13}$ imply that $Hf_3AlC_2$ should be prone to shear along the crystallographic *b*- and *c*-axis, when a significant force is applied to the crystallographic *a*-axis. As mentioned above, the elastic constant $C_{44}$ is a measure of the shear resistance and in this study it is surprisingly equal to the shear modulus *G*.

**Table 2.** The calculated elastic constants $C_{ij}$ (GPa), bulk modulus *B* (GPa), shear modulus *G* (GPa), Young's modulus *Y* (GPa), Pugh ratio *G/B*, and Poisson ratio ν of the $Hf_3AlC_2$ MAX phase.

| $C_{11}$ | $C_{12}$ | $C_{13}$ | $C_{33}$ | $C_{44}$ | *B* | *G* | *Y* | *G/B* | *ν* | Ref. |
|---|---|---|---|---|---|---|---|---|---|---|
| 347 | 77 | 80 | 291 | 127 | 162 | 127 | 302 | 0.78 | 0.189 | This |
| 357 | 82 | 83 | 283 | 126 | 166 | 128 | 305 | 0.77 | 0.193 | [29] |
| 348 | 79 | 82 | 290 | 112 | 163 | 121 | 291 | 0.74 | 0.203 | [41] |

The bulk and shear modulus are two important properties of polycrystalline materials. The bulk modulus $B$ measures the strength of the inter-atomic bonding and the resistance to volume deformation in solids. The rather high bulk modulus of $Hf_3AlC_2$ indicates the strength of its chemical bonds and its ability to resist volume deformation. The bulk modulus $B$ along with the shear elastic constant $C_{44}$ can be used to assess the machinability of compounds. The machinability index, as defined by Sun *et al*. [48] is $\mu = B/C_{44}$. The high bulk modulus together with a low shear resistance should make $Hf_3AlC_2$ easily machinable. The shear modulus $G$ can be used to explain how a material resists transverse (plastic) deformations. It can also quantify the average shearability of a material. The large value of $G$ implies that the ternary ceramic $Hf_3AlC_2$ should resist the shear forces, which are acting during machining.

The shear modulus to bulk modulus ratio $G/B$ is probably as important as $B$ and $G$ separately. Using this ratio, Pugh [49] in 1954 first classified the solid materials into two categories: brittle and ductile. Pugh also predicted a critical value of 0.57 for $G/B$ that separates the brittle compounds from ductile ones. A material is characterized as brittle if the Pugh's ratio, $G/B$ is greater than 0.57; otherwise, the material exhibits ductile nature. As the calculated value (0.78) of $G/B$ is greater than 0.57, $Hf_3AlC_2$ should be a brittle material.

The Young's modulus $Y$ evaluates the response to a uniaxial stress taking average over all directions. A material's stiffness depends mostly on its Young's modulus. It can be obtained from the bulk and shear moduli via the equation: $Y = 9BG/(3B + G)$. A large value of 302 GPa for $Hf_3AlC_2$ indicates that it is a significantly stiff ceramic.

The Poisson's ratio $v$ is another essential tool for understanding the mechanical behaviors of solids. The bulk and shear moduli provide the Poisson's ratio via the equation $v = (3B - 2G)/(6B + 2G)$. It can be used to predict the stability of materials against shear. Small values of this parameter for $Hf_3AlC_2$ indicate its stability against shear [50]. The Poisson's ratio can also be used to assess the nature of interatomic forces in crystals [51]. Poisson's ratios ranging from 0.25 to 0.50 are mainly associated with central force solids. Conversely, non-central force solids are those that possess Poisson's ratios outside of this range. Clearly, the 312 MAX phase $Hf_3AlC_2$ belongs to the latter group with $v \sim 0.2$. Again, the Poisson's ratio $v$ can be used to determine the failure mode of solids. Brittle failure occurs for materials that have Poisson's ratio less than 0.26 and ductile failure is associated with the materials for which $v > 0.26$ [52,53]. In addition, the Poisson's ratio is an essential tool for assessing the nature of chemical bonding in crystals. A material is characterized by covalent bonds if $v = 0.1$ and metallic bond leads to atomic bonding when $v = 0.33$ [54]. The Poisson's ratio of $Hf_3AlC_2$ lies within these two characteristic values. For this reason, the chemical bonding in the newly synthesized $Hf_3AlC_2$ is expected to be a combination of covalent and metallic in nature.

### *3.2.2. Elastic anisotropy*

Elastic anisotropy is inherent to the nature of crystalline solids. It plays a determining role in many physical properties of materials such as phase transformations, atypical phonon modes, anisotropic plastic deformation, precipitation, dislocation dynamics, mechanical yield points, elastic instability, crack behavior, anisotropy in chemical bonding between atoms in different planes and internal friction [55]. Elastic anisotropy has also fascinating application in Geophysics. Therefore, the study of elastic anisotropy is very important. Though cubic crystals have only a Zener anisotropy index, hexagonal crystals have a number of elastic anisotropy factors. Due to three independent shear elastic tensors, the hexagonal crystals like $Hf_3AlC_2$ have three types of shear anisotropy factors [56]. The shear anisotropy factor for {100} shear planes between the ⟨011⟩ and ⟨010⟩ directions is

$$A_1 = \frac{(C_{11} + C_{12} + 2C_{33} - 4C_{13})}{6C_{44}},$$

for {010} shear planes between the ⟨101⟩ and ⟨001⟩ directions, it is

$$A_2 = \frac{2C_{44}}{C_{11} - C_{12}},$$

and finally for {001} shear planes between the ⟨110⟩ and ⟨010⟩ directions, it is

$$A_3 = \frac{(C_{11} + C_{12} + 2C_{33} - 4C_{13})}{(C_{11} - C_{12})}$$

For isotropic crystals $A_i$'s ($i$ = 1, 2, 3) are all equal to unity. The factors $A_i$ possess a value larger or smaller than unity when the crystal systems are anisotropic. The deviation of $A_i$ from unity is a measure of the degree of elastic anisotropy. The obtained values for shear anisotropy factors shown in Table 3 suggest that the title compound $Hf_3AlC_2$ is elastically anisotropic, being highest for {001} shear planes.

**Table 3.** Anisotropic factors $A_1$, $A_2$, $A_3$, and $k_c/k_a$, percentage anisotropy factors $A_G$, and $A_B$, and universal anisotropic index $A^U$ of $Hf_3AlC_2$.

| $A_1$ | $A_2$ | $A_3$ | $k_c/k_a$ | $A_B$ | $A_G$ | $A^U$ | Ref. |
|---|---|---|---|---|---|---|---|
| 0.90 | 0.94 | 0.85 | 1.25 | 0.28 | 0.25 | 0.03 | This |
| 0.89 | 0.92 | 0.84 | 1.37 | 0.53 | 0.40 | 0.05 | [29]* |
| 1.01 | 0.83 | 0.84 | 1.26 | 0.30 | 0.45 | 0.05 | [41]* |

*Calculated from published data

Another factor $k_c/k_a$ is frequently used to reckon the elastic anisotropy, where $k_a$ and $k_c$ are the linear compressibility coefficients along the *a*- and *c*-axis, respectively. For hexagonal crystals, it is defined as: $k_c/k_a = (C_{11} + C_{12} - 2C_{13})/(C_{33} - C_{13})$ [57]. All the calculated values of $k_c/k_a$ are greater than unity (see Table 3), indicating the higher compressibility along the *c*-direction than that along the *a*-direction.

We have also evaluated the percentage anisotropy in compression and shear using the following equations [58]:

$$A_B = \frac{B_V - B_R}{B_V + B_R} \times 100\%$$

and

$$A_G = \frac{G_V - G_R}{G_V + G_R} \times 100\%$$

where, *B* and *G* refer to the bulk and shear moduli and their subscripts *V* and *R* refer to the Voigt and Reuss limits, respectively. Both $A_B$ and $A_G$ vary from 0 to 100%. These two terminal values indicate the material's isotropic and maximum possible anisotropic nature, respectively. It is evident from Table 3 that the anisotropy in compression and shear are small. The so-called universal anisotropy index $A^U = 5(G_V/G_R) + (B_V/B_R) - 6$ is also calculated. This index has either zero or positive value, zero representing completely isotropic crystals and positive value indicating the anisotropy of crystals [59]. The calculated value of $A^U$ is positive and very close to zero, indicating slight anisotropy in elastic properties of $Hf_3AlC_2$.

### *3.2.3. Theoretical Vickers Hardness*

Hardness is the property of a solid that highlights the resistance to plastic deformation, indentation, penetration and scratching. Hardness is fundamental from an engineering viewpoint as the resistance to wear by either friction or erosion by steam, water and oil usually increases with hardness. The theoretical hardness depends on the formalism carried out for calculations. Hardness of partially metallic compounds can be calculated with the formalism due to F. M. Gao [60]. For non-metallic covalent materials this approach has been reformulated by Gou *et al*. [61]. According to Gou *et al*., the bond hardness is calculated as:

$$H_v^\mu = 740\left(P^\mu - P^{\mu'}\right)(v_b^\mu)^{-5/3}$$

In the above equation, $P^\mu$ denotes the Mulliken population of a bond of type $\mu$, $P^{\mu'}$ refers to the metallic population and it can be determined with the volume *V* of the unit cell and the number of free electrons in a cell $n_{free} = \int_{E_P}^{E_F} N(E)dE$ as $P^{\mu'} = n_{free}/V$, $E_P$ and $E_F$ representing the energy at the pseudogap and Fermi level, respectively, and $v_b^\mu$ is the volume of a $\mu$-type bond that can be determined with the bond length $d^\mu$of type $\mu$ and the number of ν-type bonds $N_b^\nu$ per unit volume using the equation $v_b^\mu = (d^\mu)^3 / \sum_\nu [(d^\mu)^3 N_b^\nu]$. For crystals with complex multibands, the hardness can be obtained as a geometric average of all bond hardnesses as follows [62,63]:

$$H_V = [\prod^{\mu}(H_v^\mu)^{n^\mu}]^{1/\Sigma n^\mu}$$

where $n^{\mu}$ refers to the number of $\mu$-type bonds with which the multiband crystal is composed of. Considering only positive populations between the nearest atoms in the first coordination shells, the hardness value of $Hf_3AlC_2$ is calculated and listed in Table 4 along with related parameters. The calculated Vickers hardness is 4.9 GPa. This value is quite reasonable for MAX phase compounds (2–8 GPa), indicating that the newly synthesized $Hf_3AlC_2$ should be soft and easily machinable like most other MAX phases.

**Table 4.** Calculated bond number $n^{\mu}$, bond length $d^{\mu}$, bond overlap population $P^{\mu}$, metallic population $P^{\mu'}$, bond volume $v_b^{\mu}$ and bond hardness $H_v^{\mu}$ of $\mu$-type bond and Vickers hardness $H_v$ of $Hf_3AlC_2$.

| Bond | $n^{\mu}$ | $d^{\mu}$ (Å) | $P^{\mu}$ | $P^{\mu'}$ | $v_b^{\mu}$ (Å$^3$) | $H_v^{\mu}$ (GPa) | $H_v$(GPa) |
|---|---|---|---|---|---|---|---|
| Hf–C | 4 | 2.27173 | 1.46 | 0.0716 | 10.6137 | 20.0437 | 4.9 |
| Hf–C | 4 | 2.38140 | 1.02 | 0.0716 | 15.6203 | 7.1904 | |
| Hf–Al | 4 | 3.00404 | 0.78 | 0.0716 | 47.3279 | 0.8466 | |

### *3.3. Electronic properties*

#### *3.3.1 Band structure and DOS*

Knowledge of electronic band structure is essential for understanding the optical spectra and transport properties of solids. The energy band structure of $Hf_3AlC_2$, calculated using the high-symmetry points in *k*-space for a hexagonal lattice, is shown in Fig. 2a. The horizontal dashed line corresponds to the Fermi level $E_F$, representing the energy of the highest filled states at $T$ = 0 K. A few valence bands are seen to cross the Fermi level (black color) along the K–Γ and Γ–M directions and overlap with conduction bands, giving rise to a finite total density of states (DOS) at $E_F$. Accordingly, no band gap exists at $E_F$ and the new member in 312 MAX family, $Hf_3AlC_2$, should exhibit metallic conductivity. The band structure, in the vicinity of the Fermi level, is significantly anisotropic with slight *c*-axis dispersion, indicating likely anisotropy in electrical conductivity and other electronic properties of the newly synthesized $Hf_3AlC_2$.

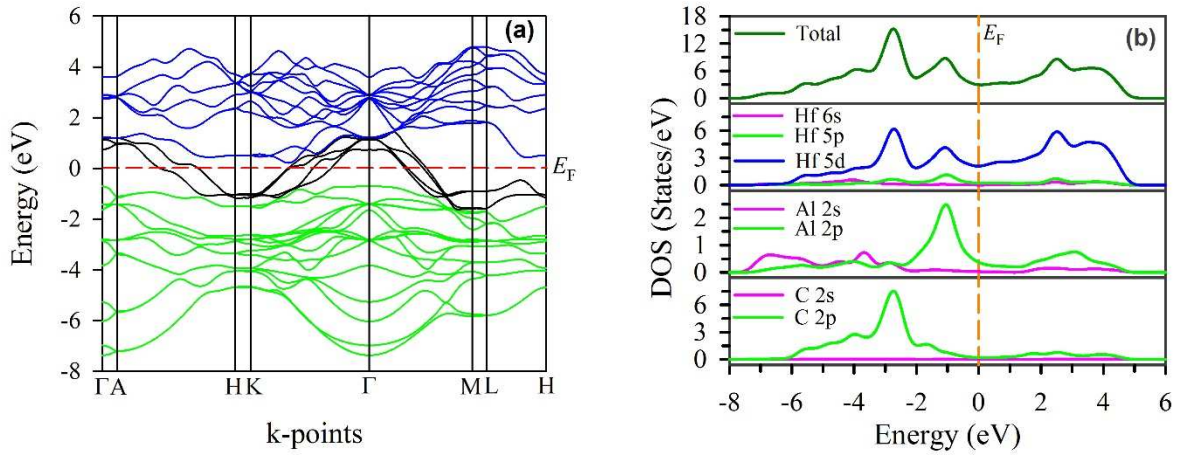


**Fig. 2.** (a) Electronic band structure and (b) Total and partial DOS of $Hf_3AlC_2$.

We have also calculated the total as well as partial density of states (DOS) to explain the electronic structure and chemical bonding in $Hf_3AlC_2$ as shown in Fig. 2b. The Fermi level, $E_F$ is set at 0 eV in the energy scale and represented by the orange vertical dotted line. The value of the DOS at the Fermi level is found to be 2.95 states per eV per unit cell. The DOS at $E_F$ mainly originates from the Hf-5*d* states, which is about 71% of the total DOS. This d-resonance and the finite value of DOS at $E_F$, indicates again the metallic conductivity of the ternary compound $Hf_3AlC_2$. Also, the antibonding states above the Fermi level are dominated by Hf-5*d* states. The wide valence band consists of three distinct parts. The lower part extends from –7.6 eV to –3.4 eV and contains two minor peaks. The middle part consists of a highest peak located between –3.4 to –2.0 eV is originated from the strong hybridization between Hf 5d and C 2p electrons. This hybridization leads to form strong covalent Hf–

C bonding in $Hf_3AlC_2$. The higher part of the valence band extends from –2.0 eV to the Fermi level and contains a low peak due to Hf-5*d* and Al-2*p* states. As a result, a weak covalent Hf–Al bonding exists. Moreover, some ionic character in chemical bonding is expected because of the difference in electronegativity among the constituent elements. From the above discussion, the chemical bonding in $Hf_3AlC_2$ can be explained as a combination of metallic, covalent and ionic contributions.

### *3.3.2. Mulliken populations*

Mulliken population analysis is an extensively used method for analyzing the electronic structure calculations performed with Linear Combination of Atomic Orbitals (LCAO) basis sets. In the CASTEP interface, this analysis is accomplished with a projection of the planewave states onto a localized basis with a method proposed by Sanchez-Portal *et al*. [64]. Population analysis of the resulting projected states is then employed with the Mulliken formalism [65]. Mulliken population analysis generates Mulliken charges, Mulliken bond populations and Hirshfeld charges for non-magnetic materials. In addition to offering an ideal condition for atomic bonding, the overlap population can be useful to evaluate the ionic or covalent character of a chemical bond. A covalent bond can be identified with a high value of the bond population. Conversely, an ionic bond is indicated by a low value. A different gauge of ionic character of chemical bonding can be obtained from the effective ionic valence that represents an absolute difference of the formal ionic charge from the Mulliken charge assigned with the anion species. A zero value for the effective valence specifies a totally ionic bond, while a value greater than zero is a sign of growing levels of covalency. Positive and negative populations indicate the bonding and antibonding states, respectively. The calculated bond overlap population between the nearest atoms in the first coordination shells and effective valence is listed in Table 5. It is evident from Table 5 that the atomic bonding in $Hf_3AlC_2$ is dominated by covalent bonds. Among different bonds, Hf1–C, Hf2–C, and Hf1–Al are covalent with order Hf1–C > Hf2–C > Hf1–Al. The reverse of this order will signify the order of ionicity level of the chemical bonds because a high overlap suggests a low degree of ionicity in the atomic bond. The ionicity can be evaluated with the formalism proposed by He *et al*. [66] as follows: $P_i = 1 - \exp[-|P_c - P^\mu|/P^\mu]$, where $P^\mu$ refers to the overlap population of a $\mu$-type bond and $P_c$ denotes the bond population for an ideal covalent bond. The value of ionicity index $P_i$ varies from zero to unity, zero representing completely covalent bond and unit value indicating the purely ionic bond. In this calculation, a value of $P_c$ equal to two is taken to correspond to a totally covalent bond. The calculated $P_i$ value for Hf1–C, Hf2–C, and Hf1–Al bonds are 0.31, 0.62, and 0.79, respectively, indicating the ionicity level of three bonds. The level of metallicity of the bond can be defined as $f_m = P^{\mu'}/P^\mu$ [61,67]. The bond Hf1–C, Hf2–C and Hf1–Al possess metallicities of 0.0490, 0.0702, and 0.0918, respectively, signifying that the Hf1–Al bond is highly metallic compared to other bonds.

**Table 5.** Mulliken atomic and bond overlap population of $Hf_3AlC_2$.

| Mulliken atomic population | | | | | | |
|---|---|---|---|---|---|---|
| Atoms | *s* | *p* | *d* | Total | Charge (e) | Effective valence charge (e) |
| C | 1.56 | 3.32 | 0.00 | 4.88 | -0.88 | -- |
| Al | 1.17 | 1.99 | 0.00 | 3.15 | -0.15 | 2.85 |
| Hf (1) | 0.40 | -0.02 | 2.74 | 3.12 | 0.88 | 3.12 |
| Hf (2) | 0.41 | 0.30 | 2.77 | 3.48 | 0.52 | 3.48 |
| Mulliken bond overlap population (metallic population $P^{\mu'} = 0.0716$) | | | | | | |
| Bond | Bond Number $n^\mu$ | Bond length $d^\mu$ (Å) | Bond population $P^\mu$ | Bond covalency (%) | Bond ionicity (%) | Bond metallicity (%) |
| Hf1–C | 4 | 2.27173 | 1.46 | 73 | 31 | 4.90 |
| Hf2–C | 4 | 2.38140 | 1.02 | 51 | 62 | 7.02 |
| Hf1–Al | 4 | 3.00404 | 0.78 | 39 | 79 | 9.18 |

*3.3.3. Charge density and Fermi surface*

The charge density associated with the bonding atoms corresponds to the net shared charge as atoms are brought together to form crystalline solids. In an attempt to give a clear picture of the bonding nature, the calculated charge density distributions along (010) planes are plotted in Fig. 3. The adjacent scale indicates the high and low density of electronic charge with blue and red colors, respectively. The contour map of charge density includes and identifies areas with accumulation and depletion of electronic charge. Covalent bonding between two atoms can be guessed with high accumulation of electronic charges between them. Ionic bonds can be identified with the negative and positive charge balance at the relevant atoms positions [68]. It is evident from Fig. 3 that strong covalent bonds occur between C and Hf atoms. A comparatively weaker covalent bonding between Al and Hf atoms is also observed.

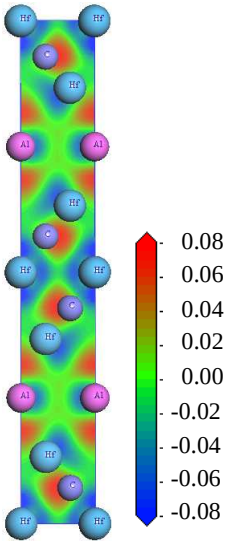


**Fig. 3.** Charge density distribution of $Hf_3AlC_2$ along (010) planes.

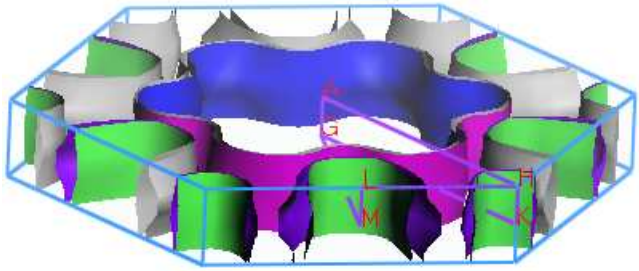

**Fig. 4.** Fermi surface topology of $Hf_3AlC_2$.

The Fermi surface of $Hf_3AlC_2$ is displayed in Figure 4. It consists of both electron- and hole-like sheets. The hole-like sheets of prismatic-like topology are coaxial with the Γ–A direction. Conversely, the electron-like sheets are complex enough and centered in the corners of the Brillouin zone. Quasi-two-dimensional-like topology (colored with blue and pink) due to low-dispersive bands is a main feature of the Fermi surface of $Hf_3AlC_2$. Similar topology is assumed to be responsible for superconductivity in $Mo_2GaC$ and no such topology is found in non-superconducting $Nb_2GaC$ and $V_2GaC$ [69]. Moreover, an additional roughly cylindrical sheet appears coaxial with the L-M direction, which is also observed in superconducting $Nb_2SnC$ phase but not in non-superconducting $Ti_2SnC$, $Zr_2SnC$ and $Hf_2SnC$ phases [70]. These similarities indicate the possible superconductivity of $Hf_3AlC_2$. If this is experimentally confirmed in the future, $Hf_3AlC_2$ will be the first superconducting member in the 312 MAX family.

*3.4. Optical Properties*

The optical properties of crystalline solids can be explained with a complex dielectric function, expressed as $\varepsilon(\omega) = \varepsilon_1(\omega) + i\varepsilon_2(\omega)$, where the real $\varepsilon_1(\omega)$ and the imaginary $\varepsilon_2(\omega)$ parts follow Kramers–Kronig relations. It is known that the imaginary part $\varepsilon_2(\omega)$ of the dielectric function is required as initial condition to calculate the rest of the optical constants [18]. The imaginary part of the dielectric constant is determined from the momentum matrix elements related to the occupied and unoccupied wave functions in accordance with the selection rules [71] and can be formulated as:

$$\varepsilon_2(\omega) = \frac{2e^2\pi}{\Omega\varepsilon_0} \sum_{k,v,c} |\langle \psi_k^c | \boldsymbol{u} \cdot \boldsymbol{r} | \psi_k^v \rangle|^2 \, \delta(E_k^c - E_k^v - E)$$

In this formula, $\omega$ denotes the frequency of photon, $e$ refers to the electronic charge, $\Omega$ represents the volume of a unit cell, $\boldsymbol{u}$ denotes the unit vector along the polarization of the incident electric field and $\psi_k^c$ and $\psi_k^v$ are respective wave functions for conduction and valence band electrons at a particular $k$. The real part of the dielectric function can be derived from the imaginary part using the Kramers-Kronig transformation. Other remaining optical functions, such as the refractive index $n(\omega)$, extinction coefficient $k(\omega)$, absorption coefficient $\alpha(\omega)$, energy-loss spectrum $L(\omega)$, optical conductivity $\sigma(\omega)$ and reflectivity $R(\omega)$, can be obtained from both the real and imaginary parts of the dielectric functions $\varepsilon_1(\omega)$ and $\varepsilon_2(\omega)$ as described in the literature [18]. Due to the metallic nature of $Hf_3AlC_2$, a Drude term [72] including 3 eV as unscreened plasma frequency and 0.05 eV as damping are incorporated in all computations. In all optical calculations, 0.5 eV is chosen as the smearing value. All optical functions are calculated for two polarization directions [100] and [001] with photon energies ranging from 0 to 20 eV.

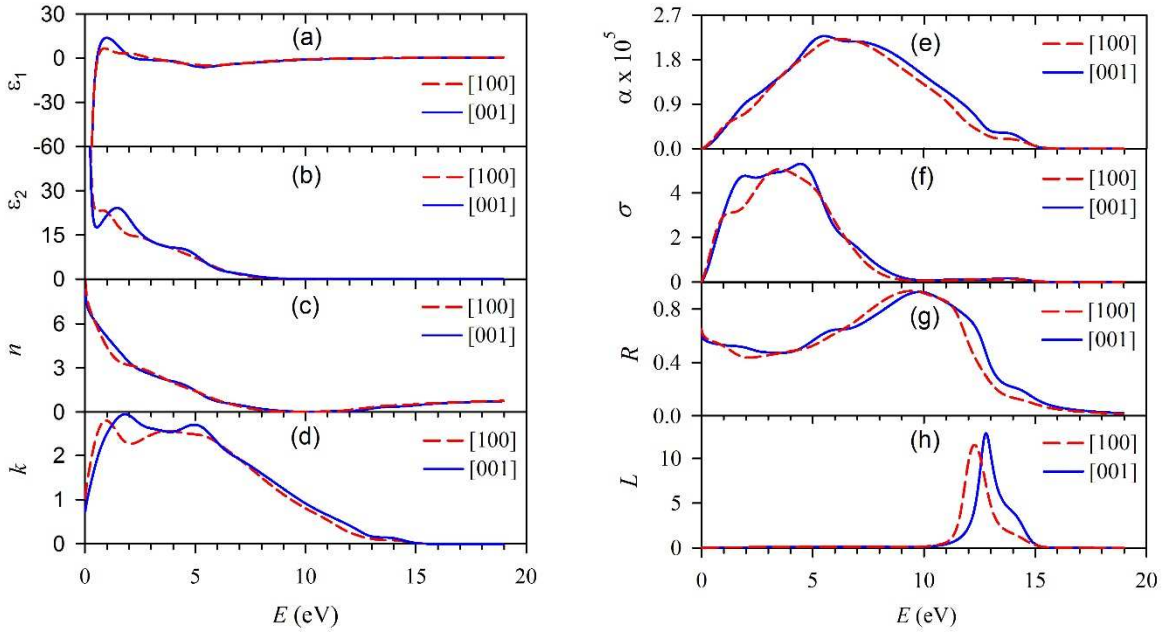


**Fig. 5.** Energy dependence of (a) real part of dielectric function, (b) imaginary part of dielectric function, (c) refractive index, (d) extinction coefficient, (e) absorption coefficient, (f) photo conductivity, (g) reflectivity, (h) loss function of $Hf_3AlC_2$ for two polarization directions.

The dielectric function is the dominant optical property of crystals. The evaluated real part of the dielectric function of $Hf_3AlC_2$ for two different polarization directions is depicted in Fig. 5a. In the low energy range, the real part $\varepsilon_1(\omega)$ of the dielectric function is found to pass through zero from below (negative values), indicating the metallic nature of $Hf_3AlC_2$. In the whole energy range, similar features are observed in the spectra due to both polarizations, except for the energy range of 0.8–1.8

eV. Small differences in the intensity of a single peak centered at 0.9 eV in the $\varepsilon_1(\omega)$ spectra reveal slightly anisotropic optical properties of $Hf_3AlC_2$ in the low photon energy range.

The imaginary part $\varepsilon_2(\omega)$ of the dielectric function is another fundamental characteristic of the optical properties of crystals. For two polarizations of incident photons, the investigated $\varepsilon_2(\omega)$ is shown in Fig. 5b. It is seen that the imaginary part $\varepsilon_2(\omega)$ comes close to zero from above, which assures again the metallic nature of $Hf_3AlC_2$. Only one low peak is observed in each spectra of $\varepsilon_2(\omega)$, which is caused by transitions of orbital electrons. The intra-band transitions are responsible for the peaks in the low energy region. Conversely, the peaks, in the high energy region, arise as a result of the inter-band transition of electrons.

Appropriate knowledge regarding the refractive index $n(\omega)$ of crystals is an indispensable guide to perfect design of electronic appliances. The static value of the refractive index $n(0)$ for both polarization directions is same with a value of 8.5. In the moderate-infrared region, a sharp rise due to intra-band transitions of electrons is seen in each spectrum. The spectra of $n(\omega)$ exhibit a continuous decrease starting at 0.1 eV and attain a lowest value of 0.02 at around 10 eV. The spectra then increase and reach a value of 0.8 at 20 eV. The refractive spectra are evidence for slight anisotropy extended from 0.6 to 2.0 eV.

The extinction coefficient $k(\omega)$ estimates the absorption loss while the electromagnetic radiation propagates through an optical medium. The calculated extinction coefficient of $Hf_3AlC_2$ for two different polarization directions is shown in Fig. 5d. A small anisotropy is observed when photons carry energies of 0 to 5.8 eV. A sharp rise above 0 eV is caused by intra-band transitions of electrons. The local maxima on the spectra of $k(\omega)$ correspond to the zero value of $\varepsilon_1(\omega)$.

The coefficient of absorption $\alpha$ estimates the penetration depth into a material for light rays of a given wavelength (energy) before being absorbed and gives useful information regarding efficiency for optimum solar energy conservation. The calculated absorption spectra plotted in Fig. 5e begin at zero photon energy as $Hf_3AlC_2$ is metallic in nature. The absorption spectra for both polarization directions increase with photon energy to attain the highest values at 6 and 5.3 eV in the ultra violet region for polarization in [100] and [001] directions, respectively, indicating $Hf_3AlC_2$ is a promising material for absorbing. Further increase of photon energy gives rise to a decrease of the absorption coefficient. The absorption spectra for both polarizations exhibit slight anisotropy in almost the entire range of photon energies.

The optical conductivity corresponds to the electrical conductivity when an alternating electric field exists. The calculated real part of the optical conductivity $\sigma$ is depicted in Fig. 5f. It is observed that $Hf_3AlC_2$ should be highly conductive electrically when incident photons carry energies of 3.3 and 4.4 eV for polarization in [100] and [001] directions, respectively. The optical conductivity shows evidence of small anisotropy for photon energies ranging from 1–5.2 eV. In addition, a difference in peak height is observed for the two different polarizations.

The reflectivity $R$ represents the fraction of energy from a wave striking the surface of a material that is possessed by the wave reflected from the surface. The calculated optical reflectivity $R(\omega)$ is shown in Fig. 5g. The reflectivity spectra show a drastic increase in both moderate infrared and ultra-violet regions to arrive at the highest values of ~91%. No considerable change is observed in the visible light region (~1.8–3.1 eV) and the reflectivity spectra keep above 44%, which should make $Hf_3AlC_2$ a contestant material for coatings to reduce solar heating [73]. Moreover, the compound $Hf_3AlC_2$ is expected to appear as metallic gray because of their almost unvarying reflectivity in the visible light region. The reflectivity spectra show slight anisotropy in the entire range of photon energies.

The energy loss function $L(\omega)$ evaluates the energy loss of fast electrons passing through the material. The calculated energy loss spectra plotted in Fig. 5h exhibit no peaks within the range of energies 0–11 eV because of the large $\varepsilon_2(\omega)$ [74]. A large peak on both spectra due to plasma oscillations is seen in the range of energies 11–15 eV. The highest peak is also associated with a characteristic frequency, well-known as the bulk plasma frequency. At this frequency, the spectra of $\varepsilon_1(\omega)$ become extinct and the material switches from metallic to dielectric response [72,75]. From the spectra of $L(\omega)$ for the polarization directions [100] and [001], the bulk plasma frequencies of $Hf_3AlC_2$ are expected to be 12.2 and 12.9 eV, respectively. A rapid decline in reflectivity is seen to

occur at this frequency as shown in Fig. 5g. When the frequency of the incident light is higher than the plasma frequency, $Hf_3AlC_2$ is expected to be a transparent material [32].

### *3.5. Lattice dynamics*

In order to verify the dynamical stability of $Hf_3AlC_2$, the phonon dispersion along with phonon density of states (PHDOS) are also investigated. The calculated phonon dispersion curve, shown in Fig. 6a, at the equilibrium volume for $Hf_3AlC_2$ along the high-symmetry directions displays no evidence of negative phonon frequencies in the entire Brillouin zone. This confirms the dynamical stability of $Hf_3AlC_2$ against mechanical perturbations at normal pressure. Accordingly, the Gibbs free energy of the system corresponds to a local minimum regarding small vibrations of the lattice. This 'intrinsic stability' is a necessary decisive factor for a stable phase. There are six atoms in the primitive cell of $Hf_3AlC_2$, which leads to eighteen phonon branches including fifteen optical modes and three acoustic modes. The lower branches in the dispersion curve are defined as the acoustic branches. While k is small, the acoustic dispersion is of the form $\omega = vk$, which represents the $\omega$-k relationship of sound waves. Coherent vibrations of atoms within a lattice outside their equilibrium positions produce the acoustic phonons. The upper branches are defined as the optical branches. They control most optical properties of solids. The out-of-phase oscillations of atoms in a lattice, being one atom moves to the left, and its neighbor to the right, produce optical phonons. They are named optical for the reason that in most ionic crystals they are easily stimulated with infrared radiation leading to a vibrational state in which both negative and positive ions oscillate out of phase with each other. The acoustic modes inherently have zero frequencies at the Γ point. The three acoustic branches of the phonon dispersion overlap with the lower optical branches and as a result no phononic band gap exists between acoustic and optical modes in the PHDOS.

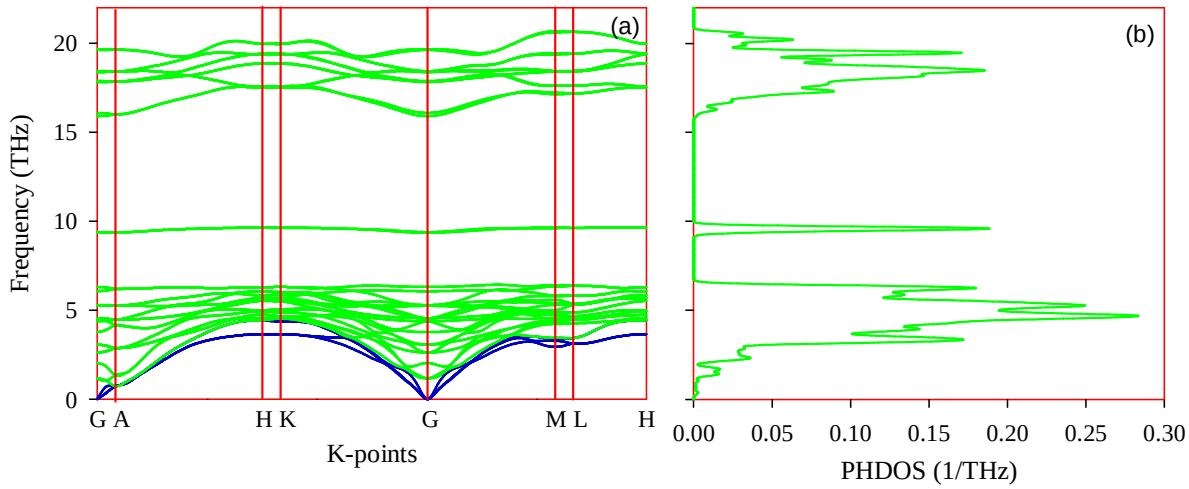


**Fig. 6.** (a) Phonon dispersion curves and (b) phonon density of states of $Hf_3AlC_2$.

The calculated total phonon density of states (PHDOS) for $Hf_3AlC_2$ is shown in Fig. 6b. The peaks in PHDOS arise due to the relative flatness of the bands. Conversely, both the downward and upward sloping bands reduce the peak-heights in the total DOS. It can be clarified by considering a peak and the flatness/sloping of its corresponding bands. As for example, we can first consider the separate peak that arises due to the bands of ~9.3 THz frequency. It is obvious from the dispersion curve that the relevant bands are almost flat. Secondly, we can consider the lower bands, which are sloping in upward and produce reduced peaks in the total DOS.

### *3.6. Debye temperature*

The Debye temperature of solids is a characteristic temperature that makes possible the evaluation of numerous physical properties of crystals. These properties include thermal conductivity and expansion, lattice vibration, specific heat and melting temperature. In superconducting materials, it maintains a relation with the electron-phonon coupling constant as well as with the superconducting

transition temperature. Additionally, the vacancy formation energy in metals mostly depends on the Debye temperature. Anderson [76] proposed a simplified method based on the average sound velocity for calculating the Debye temperature. This method has become popular and is considered one of the standard methods. Following Anderson's method, it is possible to calculate $\theta_D$ as follows:

$$\theta_D = \frac{h}{k_B}\left[\left(\frac{3n}{4\pi}\right)\frac{N_A\rho}{M}\right]^{1/3} v_m$$

where $h$ and $k_B$ are the Planck's and Boltzmann's constants, respectively, $N_A$ is the Avogadro's number, $\rho$ is the mass density, $M$ refers to the molecular weight and $n$ denotes the number of atoms in the molecule. In a polycrystalline solid, the sound wave travels with an average velocity $v_m$, which can be calculated from

$$v_m = \left[\frac{1}{3}\left(\frac{1}{v_l^3} + \frac{2}{v_t^3}\right)\right]^{-1/3}$$

where $v_l$ and $v_t$ are the longitudinal and transverse sound velocities in a polycrystalline material, respectively. These velocities can be obtained from the polycrystalline shear modulus $G$ and the bulk modulus $B$ as follows [76]:

$$v_l = \left[\frac{3B + 4G}{3\rho}\right]^{1/2}$$

and

$$v_t = \left[\frac{G}{\rho}\right]^{1/2}$$

The calculated mass density$\rho$, sound velocities $v_l$, $v_t$, and $v_m$ and Debye temperature $\theta_D$ are listed in Table 6. Compared to other 312 MAX phases [2,77–79] and the promising thermal barrier coating (TBC) material $Y_4Al_2O_9$ [80], the Debye temperature of $Hf_3AlC_2$ is small. It means that the thermal conductivity of $Hf_3AlC_2$ is comparatively low and that it could become an even better TBC material.

**Table 6.** Calculated density ($\rho$ in gm/cm$^3$), longitudinal, transverse as well as average sound velocities ($v_l$, $v_t$, and $v_m$ in km/s) and Debye temperature ($\theta_D$ in K) of $Hf_3AlC_2$.

| $\rho$ | $v_l$ | $v_t$ | $v_m$ | $\theta_D$ | Ref. |
|---|---|---|---|---|---|
| 10.288 | 5.6750 | 3.5135 | 3.8744 | 459.9 | This calc. |
| 10.470 | 5.6706 | 3.4965 | 3.8573 | 460.5 | Calc. [29]* |
| 10.562 | 5.5414 | 3.3847 | 3.7376 | 447.6 | Calc. [41]* |

*Calculated from published data

*3.7. Thermodynamic properties*

The behavior of a system at elevated temperature can be described by different temperature-dependent thermodynamic potential functions such as the enthalpy $H(T)$, entropy $S(T)$, free energy $F(T)$ and heat capacity $C_V(T)$. These thermodynamic functions for $Hf_3AlC_2$ have been calculated at zero pressure using the quasi-harmonic approximation [81] and plotted in Fig. 7. As the Helmholtz free energy is defined by $F = H - TS$, the entropy presented as the product $T \times S$ allows comparison among the quantities $F$, $H$ and $TS$ in the same units, eV. From Fig. 7(a), it can be observed that the enthalpy, entropy and free energy have almost zero values at a temperature lower than 100K. Conversely, at temperatures above 100 K, an increase of temperature causes a considerable increase in both enthalpy and entropy but a decrease in free energy. The heat capacity $C_V$, as a function of temperature, is plotted in Fig. 7(b). It is found that the heat capacity, below temperature ~600 K, increases radically with temperature. Above this temperature, the heat capacity increases slowly and approaches the so-called asymptotic limit.

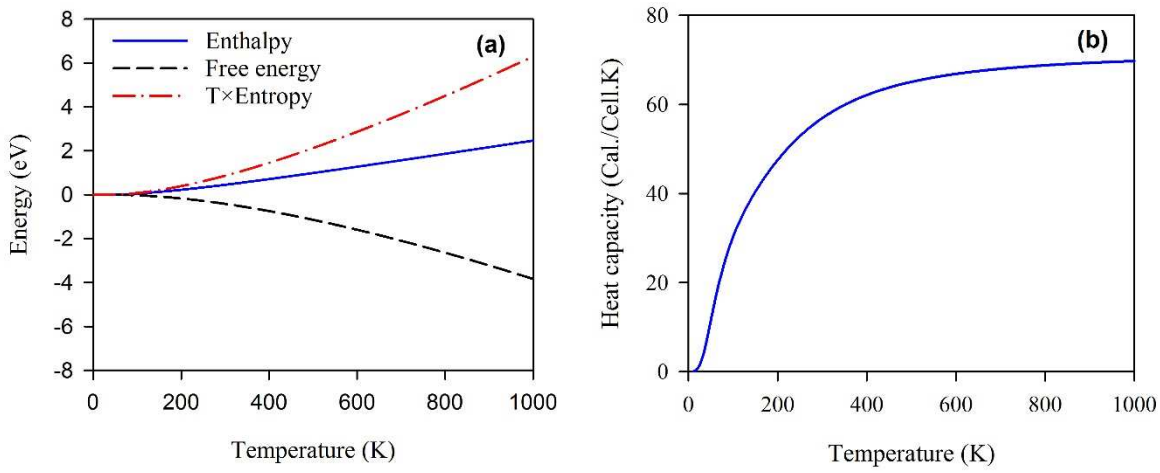


**Fig. 7.** Temperature dependence of (a) thermodynamic potential functions *H*, *F* and *TS* and (b) heat capacity $C_V$ of $Hf_3AlC_2$.

## 4. Conclusions

We have performed first principles calculations to investigate the ground state physical properties of the newly synthesized 312 MAX compound $Hf_3AlC_2$. The calculated values for the lattice parameters agree well with the corresponding experimental results. The calculated elastic constants and phonon dispersion predict the mechanical and dynamical stabilities of $Hf_3AlC_2$. A high bulk modulus together with low shear resistance and small Vickers hardness should make $Hf_3AlC_2$ a good machinable material. Large Young's modulus indicates reasonable stiffness of $Hf_3AlC_2$. A brittle nature of $Hf_3AlC_2$ can be assured from the calculated Pugh and Poison ratios along with the Cauchy pressure. This apparent contradiction, where overall metallic as well as refractory characters seem to coexist, could be behind the unique characteristic of $Hf_3AlC_2$. The newly synthesized $Hf_3AlC_2$ is suggested to be elastically anisotropic. In comparison with other 312 MAX phases, $Hf_3AlC_2$ is predicted to be a better thermal barrier coating material. The chemical bonding in $Hf_3AlC_2$ is expected to be a mixture of metallic, covalent and ionic contributions. The calculated Fermi surface topology of $Hf_3AlC_2$ indicates that it is likely a superconducting phase. Though a decrease is observed for the free energy, an increase occurs for the enthalpy and entropy with increasing temperature above 100 K. The calculated optical functions are found to be polarization dependent, providing us with a clear evidence of anisotropy in the optical properties of $Hf_3AlC_2$. The mixed bonding nature, combined with anisotropic behavior, may enhance either metallic or refractory character in specific directions and property calculations or measurements. This may be responsible for some of the average calculated mechanical properties indicating metallic character, while others appear to indicate refractory properties. Such duality is reminiscent of materials which display localized to itinerant electronic transitions [82] or are in proximity to metal to insulator transitions [83]. Therefore, a selection of mechanical properties may become an indicator for structures with potential for unusual, extraordinary properties, in a similar fashion to how they seem to single out $Hf_3AlC_2$.

## References

[1] M.W. Barsoum, The $M_{N+1}AX_N$ phases: A new class of solids: Thermodynamically stable nanolaminates, Prog. Solid State Chem. 28 (2000) 201-281.

[2] P. Finkel, M.W. Barsoum, T. El-Raghy, Low temperature dependencies of the elastic properties of $Ti_4AlN_3$, $Ti_3Al_{1.1}C_{1.8}$, and $Ti_3SiC_2$, J. Appl. Phys. 87 (2000) 1701-1703.

[3] A.S. Ingason, A. Mockute, M. Dahlqvist, F. Magnus, S. Olafsson, U.B. Arnalds, B. Alling, I.A. Abrikosov, B. Hjörvarsson, P.O.Å. Persson, J. Rosen, Magnetic self-organized atomic laminate from first principles and thin film synthesis, Phys. Rev. Lett. 110 (2013) 195502.

[4] R. Meshkian, A.S. Ingason, U.B. Arnalds, F. Magnus, J. Lu, J. Rosén, A magnetic atomic laminate from thin film synthesis: $(Mo_{0.5}Mn_{0.5})_2GaC$, APL Mater. 3 (2015) 076102.

[5] P. Eklund, M. Beckers, U. Jansson, H. Högberg, L. Hultman, The $M_{n+1}AX_n$ phases: materials science and thin-film processing, Thin Solid Films 518 (2010) 1851-1878.
[6] M.W. Barsoum, MAX phases: properties of machinable ternary carbides and nitrides, Wiley-VCH, Germany, 2013.
[7] A.S. Ingason, A. Petruhins, M. Dahlqvist, F. Magnus, A. Mockute, B. Alling, L. Hultman, I.A. Abrikosov, P.O.Å. Persson and J. Rosen, A Nanolaminated Magnetic Phase: $Mn_2GaC$, Mater. Res. Lett. 2 (2014) 89–93.
[8] B. Anasori, J. Halim, J. Lu, C.A. Voigt, L. Hultman, M.W. Barsoum, $Mo_2TiAlC_2$: A new ordered layered ternary carbide, Scr. Mater. 101 (2015) 5-7.
[9] E.a.N. Caspi, P. Chartier, F. Porcher, F. Damay, T. Cabioc'h, Ordering of (Cr,V) layers in nanolamellar $(Cr_{0.5}V_{0.5})_{n+1}AlC_n$ compounds, Mater. Res. Lett. 3 (2015) 100-106.
[10] R. Meshkian, Q. Tao, M. Dahlqvist, J. Lu, L. Hultman, J. Rosen, Theoretical stability and materials synthesis of a chemically ordered MAX phase, $Mo_2ScAlC_2$, and its two-dimensional derivate $Mo_2ScC_2$ MXene, Acta Mater. 125 (2017) 476-480.
[11] D. Horlait, S.C. Middleburgh, A. Chroneos, W.E. Lee, Synthesis and DFT investigation of new bismuth-containing MAX phases, Sci. Rep. 6 (2016) 18829.
[12] D. Horlait, S. Grasso, A. Chroneos, W.E. Lee, Attempts to synthesise quaternary MAX phases $(Zr,M)_2AlC$ and $Zr_2(Al,A)C$ as a way to approach $Zr_2AlC$, Mater. Res. Lett. 4 (2016) 137-144.
[13] D. Horlait, S. Grasso, N. Al Nasiri, P.A. Burr, W.E. Lee, Synthesis and oxidation testing of MAX phase composites in the Cr–Ti–Al–C quaternary system, J. Am. Ceram. Soc. 99 (2016) 682-690.
[14] T. Lapauw, K. Lambrinou, T. Cabioc'h, J. Halim, J. Lu, A. Pesach, O. Rivin, O. Ozeri, E.N. Caspi, L. Hultman, P. Eklund, J. Rosén, M.W. Barsoum, J. Vleugels, Synthesis of the new MAX phase $Zr_2AlC$, J. Eur. Ceram. Soc. 36 (2016) 1847-1853.
[15] T. Lapauw, J. Halim, J. Lu, T. Cabioc'h, L. Hultman, M.W. Barsoum, K. Lambrinou, J. Vleugels, Synthesis of the novel $Zr_3AlC_2$ MAX phase, J. Eur. Ceram. Soc. 36 (2016) 943-947.
[16] E. Zapata-Solvas, S.G. Christopoulos, N. Ni, D.C. Parfitt, D. Horlait, M.E. Fitzpatrick, A. Chroneos, W.E. Lee, Experimental synthesis and DFT investigation of radiation tolerance of $Zr_3(Al_{1-x}Si_x)C_2$ MAX phases, J. Am. Ceram. Soc. 100 (2017) 1377-1387.
[17] E. Zapata-Solvas, M.A. Hadi, D. Horlait, D.C. Parfitt, A. Thibaud, A. Chroneos, W.E. Lee, Synthesis and physical properties of $(Zr_{1-x},Ti_x)_3AlC_2$ MAX phases, J. Am. Ceram. Soc. 100 (2017) 3393-3401.
[18] M.A. Hadi, R.V. Vovk, A. Chroneos, Physical properties of the recently discovered $Zr_2(Al_{1-x}Bi_x)C$ MAX phases, J. Mater. Sci. Mater. Electron. 27 (2016) 11925-11933.
[19] M.A. Hadi, M. Roknuzzaman, F. Parvin, S.H. Naqib, A.K.M.A. Islam, M. Aftabuzzaman, New MAX phase superconductor $Ti_2GeC$: A first-principles study, J. Sci. Res. 6 (2014) 11-27.
[20] M.S. Ali, F. Parvin, A.K.M.A. Islam, M.A. Hossain, Newly synthesized nanolaminate $Nb_2GeC$: Hardness, thermodynamic and optical properties by first-principles method, Comput. Mater. Sci. 74 (2013) 119-123.
[21] Z. Liu, E. Wu, J. Wang, Y. Qian, H. Xiang, X. Li, Q. Jin, G. Sun, X. Chen, J. Wang, Crystal structure and formation mechanism of $(Cr_{2/3}Ti_{1/3})_3AlC_2$ MAX phase, Acta Mater. 73 (2014) 186-193.
[22] M.A. Hadi, M. Roknuzzaman, A. Chroneos, S.H. Naqib, A.K.M.A. Islam, R.V. Vovk, K. Ostrikov, Elastic and thermodynamic properties of new $(Zr_{3-x}Ti_x)AlC_2$ MAX-phase solid solutions, Comput. Mat. Sci. 137 (2017) 318-326.
[23] M.A. Ali, M.T. Nasir, M.R. Khatun, A.K.M.A. Islam, S.H. Naqib, An ab initio investigation of vibrational, thermodynamic, and optical properties of $Sc_2AlC$ MAX compound, Chin. Phys. B 25 (2016) 103102.
[24] M. Roknuzzaman, M.A. Hadi, M.J. Abden, M.T. Nasir, A.K.M.A. Islam, M.S. Ali, K. Ostrikov, S.H. Naqib, Physical properties of predicted $Ti_2CdN$ versus existing $Ti_2CdC$ MAX phase: An ab initio study, Comput. Mater. Sci. 113 (2016) 148-153.
[25] G. Qing-He, X. Zhi-Jun, T. Ling, Z. Xianjun, J. Guozhu, D. An, L. Rong-Feng, G. Yun-Dong, Y. Ze-Jin, Evidence of the stability of $Mo_2TiAlC_2$ from first principles calculations and its thermodynamical and optical properties, Comput. Mater. Sci. 118 (2016) 77-86.
[26] M.A. Hadi, Y. Panayiotatos, A. Chroneos, Structural and optical properties of the recently synthesized $(Zr_{3-x}Ti_x)AlC_2$ MAX phases, J. Mater. Sci. Mater. Electron. 28 (2016) 3386-3393.
[27] M.A. Ali, M.M. Hossain, N. Jahan, A.K.M.A. Islam, S.H. Naqib, Newly synthesized $Zr_2AlC$, $Zr_2(Al_{0.58}Bi_{0.42})C$, $Zr_2(Al_{0.2}Sn_{0.8})C$, and $Zr_2(Al_{0.3}Sb_{0.7})C$ MAX phases: A DFT based first-principles study, Comput. Mater. Sci. 131 (2017) 139-145.
[28] T. Lapauw, B. Tunca, T. Cabioc'h, J. Lu, P.O.A. Persson, K. Lambrinou, J. Vleugels, Synthesis of MAX phases in the Hf–Al–C system, Inorg. Chem. 55 (2016) 10922-10927.
[29] X. He, Y. Bai, C. Zhu, Y. Sun, M. Li, M.W. Barsoum, General trends in the structural, electronic and elastic properties of the $M_3AlC_2$ phases (M= transition metal): a first-principle study, Comput. Mater. Sci. 49 (2010) 691-698.

[30] A.H. Reshak, Z. Charifi, H. Baaziz, The effect of the phase transition on the optical properties of the lanthanum monopnictide compounds, J. Phys. Condens. Matter 20 (2008) 325207.
[31] M. Xu, S. Wang, G. Yin, J. Li, Y. Zheng, L. Chen, Y. Jia, Optical properties of cubic $Ti_3N$, $Zr_3N_4$, and $Hf_3N_4$, App. Phys. Lett. 89 (2006) 151908.
[32] C. Li, B. Wang, Y. Li, R. Wang, First-principles study of electronic structure, mechanical and optical properties of $V_4AlC_3$, J. Phys. D: Appl. Phys. 42 (2009) 065407.
[33] Y.L. Du, Z.M. Sun, H. Hashimoto, W.B. Tian, First-principles study on thermodynamic properties of $Ti_2AlC$ and $Ti_2SC$, Mater. Trans. 50 (2009) 2173-2176.
[34] P. Hohenberg, W. Kohn, Inhomogeneous Electron Gas, Phys. Rev. 136 (1964) B864-B871.
[35] W. Kohn, L.J. Sham, Self-consistent equations including exchange and correlation effects, Phys. Rev. 140 (1965) A1133-A1138.
[36] S.J. Clark, M.D. Segall, C.J. Pickard, P.J. Hasnip, M.I. Probert, K. Refson, M.C. Payne, First principles methods using CASTEP, Z. Kristallogr. Cryst. Mater. 220 (2005) 567-570.
[37] J.P. Perdew, K. Burke, M. Ernzerhof, Generalized Gradient Approximation made simple, Phys. Rev. Lett. 77 (1996) 3865-3868.
[38] D. Vanderbilt, Soft self-consistent pseudopotentials in a generalized eigenvalue formalism, Phys. Rev. B 41 (1990) 7892-7895.
[39] H.J. Monkhorst, J.D. Pack, Special points for Brillouin-zone integrations, Phys. Rev. B 13 (1976) 5188-5192.
[40] T.H. Fischer, J. Almlöf, General methods for geometry and wave function optimization, J. Phys. Chem. 96 (1992) 9768-9774.
[41] S. Aryal, R. Sakidja, M.W. Barsoum, W.Y. Ching, A genomic approach to the stability, elastic, and electronic properties of the MAX phases, Phys. Status Solidi B 251 (2014) 1480-1497.
[42] Y.L. Page, P. Saxe, Symmetry-general least-squares extraction of elastic data for strained materials from ab initio calculations of stress, Phys. Rev. B, 65 (2002) 104104.
[43] W. Voigt, Lehrbuch der Kristallphysik, Taubner, Leipzig, 1928.
[44] A. Reuss, Berechnung der Fließgrenze von Mischkristallen auf Grund der Plastizitätsbedingung für Einkristalle, Z. Angew. Math. Mech. 9 (1929) 49-58.
[45] R. Hill, The elastic behaviour of a crystalline aggregate, Proc. Phys. Soc. A 65 (1952) 349-354.
[46] M. Born, On the stability of crystal lattices. I, Mathematical Proceedings of the Cambridge Philosophical Society, Cambridge University Press, Cambridge, 1940, pp. 160-172.
[47] D.G. Pettifor, Theoretical predictions of structure and related properties of intermetallics, J. Mater. Sci. Technol. 8 (1992) 345-349.
[48] Z. Sun, D. Music, R. Ahuja, J.M. Schneider, Theoretical investigation of the bonding and elastic properties of nanolayered ternary nitrides, Phys. Rev. B 71 (2005) 193402.
[49] S.F. Pugh, XCII. Relations between the elastic moduli and the plastic properties of polycrystalline pure metals, The London, Edinburgh, and Dublin Philosophical Magazine and Journal of Science 45 (1954) 823-843.
[50] P. Ravindran, L. Fast, P.A. Korzhavyi, B. Johansson, J. Wills, O. Eriksson, Density functional theory for calculation of elastic properties of orthorhombic crystals: Application to $TiSi_2$, J. Appl. Phys. 84 (1998) 4892.
[51] O.L. Anderson, H.H. Demarest Jr., Elastic constants of the central force model for cubic structures: Polycrystalline aggregates and instabilities, J. Geophys. Res. 76 (1971) 1349.
[52] I.N. Frantsevich, F.F. Voronov, S.A. Bokuta, Elastic Constants and Elastic Moduli of Metals and Insulators Handbook, edited by I. N. Frantsevich, Naukova Dumka, Kiev, 1983, pp. 60-180.
[53] G. Vaitheeswaran, V. Kanchana, A. Svane, A. Delin, Elastic properties of $MgCNi_3$-a superconducting perovskite, J. Phys. Condens. Matter 19 (2007) 326214.
[54] A. Savin, D.C.H. Flad, J. Flad, H. Preuss, H.G. Schnering, On the Bonding in Carbosilanes, Angew. Chem. Int. Ed. 31 (1992) 185-187.
[55] H.M. Ledbetter, A. Migliori, A general elastic-anisotropy measure, J. Appl. Phys. 100 (2006) 063516.
[56] H.M. Ledbetter, Elastic properties of zinc: A compilation and a review, J. Phys. Chem. 6 (1977) 1181.
[57] J.M. Wang, J.Y. Wang, Y.C. Zhou, C.F. Hu, Phase stability, electronic structure and mechanical properties of ternary-layered carbide $Nb_4AlC_3$: an ab initio study, Acta Mater. 56 (2008) 1511-1518.
[58] D.H. Chung, W.R. Buessem, F.W. Vahldiek, S.A Mersol, Anisotropy in Single Crystal Refractory Compounds, Plenum, New York, 1968.
[59] S.I. Ranganathan, M. Ostoja-Starzewski, Universal elastic anisotropy index, Phys. Rev. Lett. 101 (2008) 055504.
[60] F. Gao, Theoretical model of intrinsic hardness, Phys. Rev. B 73 (2006) 132104.
[61] H. Gou, L. Hou, J.W. Zhang, F. Gao, Pressure-induced incompressibility of ReC and effect of metallic bonding on its hardness, Appl. Phys. Lett. 92 (2008) 241901.

[62] A. Szymański, J.M. Szymański, Hardness Estimation of Minerals Rocks and Ceramic Materials, sixth ed., Elsevier, Amsterdam, 1989.
[63] V.M. Glazov, V.N. Vigdorovid, Hardness of Metals, Izd. Metellurgiya, Moskva, 1989.
[64] D. Sanchez-Portal, E. Artacho, J.M. Soler, Projection of plane-wave calculations into atomic orbitals, Solid State Commun. 95 (1995) 685-690.
[65] R.S. Mulliken, Electronic population analysis on LCAO–MO molecular wave functions. I, J. Chem. Phys. 23 (1955) 1833-1840.
[66] Tian, Wenyan, H. Chen, Insight into the mechanical, thermodynamics and superconductor properties of NbRuB via first-principles calculation, Sci. Rep. 6 (2016) 19055.
[67] M.A. Hadi, M.S. Ali, S.H. Naqib, A.K.M.A. Islam, Band structure, hardness, thermodynamic and optical properties of superconducting $Nb_2AsC$, $Nb_2InC$ and $Mo_2GaC$, Int. J. Comput. Mater. Sci. Eng. 2 (2013) 1350007.
[68] F. Ernst, M. Rühle (Eds.), High-Resolution Imaging and Spectrometry of Materials, Springer-Verlag Berlin Heidelberg, New York, 2003.
[69] I.R. Shein, A.L. Ivanovskii, Structural, elastic, electronic properties and Fermi surface for superconducting $Mo_2GaC$ in comparison with $V_2GaC$ and $Nb_2GaC$ from first principles, Physica C, 470 (2010) 533-537.
[70] M.B. Kanoun, S. Goumri-Said, A.H. Reshak, Theoretical study of mechanical, electronic, chemical bonding and optical properties of $Ti_2SnC$, $Zr_2SnC$, $Hf_2SnC$ and $Nb_2SnC$, Comput. Mater. Sci. 47 (2009) 491-500.
[71] D.C. Harris, M.D. Bertolucci, Symmetry and Spectroscopy: An Introduction to Vibrational and Electronic Spectroscopy, first ed., Dover Publications, New York, 1989.
[72] R. Saniz, L.H. Ye, T. Shishidou, A.J. Freeman, Structural, electronic, and optical properties of $NiAl_3$: first-principles calculations, Phys. Rev. B 74 (2006) 014209.
[73] S. Li, R. Ahuja, M.W. Barsoum, P. Jena, B. Johansson, Optical properties of $Ti_3SiC_2$ and $Ti_4AlN_3$, Appl. Phys. Lett. 92 (2008) 221907.
[74] J.P. Watt, L. Peselnick, Clarification of the Hashin-Shtrikman bounds on the effective elastic moduli of polycrystals with hexagonal, trigonal, and tetragonal symmetries, J. Appl. Phys. 51 (1980) 1525.
[75] J.S. de Almeida, R. Ahuja, Electronic and optical properties of $RuO_2$ and $IrO_2$, Phys. Rev. B 73 (2006) 165102.
[76] O.L. Anderson, A simplified method for calculating the Debye temperature from elastic constants, J. Phys. Chem. Solids 24 (1963) 909-917.
[77] Y. Bai, X. He, Y. Sun, C. Zhu, M. Li, L. Shi, Chemical bonding and elastic properties of $Ti_3AC_2$ phases ($A$ = Si, Ge, and Sn): A first-principle study, Solid State Sci. 12 (2010) 1220-1225.
[78] M. Radovic, M.W. Barsoum, A. Ganguly, T. Zhen, P. Finkel, S. R. Kalidindi, E. Lara-Curzio, On the elastic properties and mechanical damping of $Ti_3SiC_2$, $Ti_3GeC_2$, $Ti_3Si_{0.5}Al_{0.5}C_2$ and $Ti_2AlC$ in the 300–1573 K temperature range, Acta Mater. 54 (2006) 2757-2767.
[79] P. Finkel, B. Seaman, K. Harrell, J. Palma, J.D. Hettinger, S.E. Lofland, A. Ganguly, M.W. Barsoum, Z. Sun, S. Li, R. Ahuja, Electronic, thermal, and elastic properties of $Ti_3Si_{1-x}Ge_xC_2$ solid solutions, Phys. Rev. B 70 (2004) 085104.
[80] Y. Zhou, H. Xiang, X. Lu, Z. Feng and Z. Li, Theoretical prediction on mechanical and thermal properties of a promising thermal barrier material: $Y_4Al_2O_9$, J. Adv. Ceram. 4 (2015) 83-93.
[81] M.T. Dove, Introduction to Lattice Dynamics, Cambridge University Press, Cambridge, 1993.
[82] J.B. Goodenough, J.S. Zhou, Localized to Itinerant Electronic Transitions in Transition-Metal Oxides with the Perovskite Structure, Chem. Mater. 10 (1998) 2980-2993.
[83] M. Imada, A. Fujimori, Y. Tokura, Metal-insulator transitions, Rev. Mod. Phys. 70 (1998) 1039.

Highlights:

1. The ground state physical properties of the newly synthesized $Hf_3AlC_2$ are calculated.

2. The mechanical and dynamical stabilities of $Hf_3AlC_2$ are predicted.

3. The new phase $Hf_3AlC_2$ may be a promising thermal barrier coating (TBC) material.

4. Fermi surface topology of $Hf_3AlC_2$ indicates that it is likely a superconducting phase.